Supporting Information for "Multigenetic Origin of the X-discontinuity Below Continents: Insights from African Receiver Functions"

Stephen Pugh[1*], Alistair Boyce[1,2], Ian D. Bastow[3], C. J. Ebinger[4], Sanne Cottaar[1]

[1]Bullard Laboratories, Department of Earth Sciences, University of Cambridge, UK

[2]Université Lyon 1, ENS de Lyon, CNRS, UMR 5276 LGL-TPE, F-69622, Villeurbanne, France

[3]Department of Earth Science and Engineering, Imperial College, London, UK

[4]Department of Earth and Environmental Sciences, Tulane University, New Orleans, LA, USA

[*]Corresponding author: Stephen Pugh, sdp43@cam.ac.uk

Contents of this file

1 Introduction

This supplement provides supporting figures and details to the main text. Section 2 provides the sources of sources data without corresponding DOIs in Table S1. Seismic networks with DOIs are detailed in the Open Research section of the main article. Section 3 gives an overview of manual quality control procedures implement post automatic quality control. Section 4 considers the data distribution of RF stacks and its impact on the quality of the stack. Section 5 assesses the different time-to-depth conversions implemented before stacking. Section 6 considers the relationship between presence of the X and the local temperature of the upper mantle for each stack. Finally, Section 7 considers the relationship between the X and lithospheric thickness for the vote map in Figure 5.

2 Seismic Networks for P-wave Receiver Functions in Africa

Network	FDSN website address
1B	http://www.fdsn.org/networks/detail/1B_2006/
BX	http://www.fdsn.org/networks/detail/BX/
TT	http://www.fdsn.org/networks/detail/TT/
XJ	http://www.fdsn.org/networks/detail/XJ_2002/
XJ	http://www.fdsn.org/networks/detail/XJ_2007/
XM	http://www.fdsn.org/networks/detail/XM_2002/
YF	http://www.fdsn.org/networks/detail/YF_2010/
YJ	http://www.fdsn.org/networks/detail/YJ_2001/
YK	http://www.fdsn.org/networks/detail/YK_2000/
YW	http://www.fdsn.org/networks/detail/YW_2002/
YZ	http://www.fdsn.org/networks/detail/YZ_2005/
ZC	http://www.fdsn.org/networks/detail/ZC_2001/
ZF	http://www.fdsn.org/networks/detail/ZF_2007/
ZP	http://www.fdsn.org/networks/detail/ZP_2010/
ZQ	http://www.fdsn.org/networks/detail/ZQ_2006/
ZU	http://www.fdsn.org/networks/detail/ZU_2008/

Table 1. Data for this project were downloaded for a range of networks using the Incorporated Research Institutions for Seismology (IRIS) Data Management System. The networks used with associated DOIs are detailed in the Open Research section of the main article. Those listed here do not have associated DOIs and their corresponding websites are written alongside.

Table S1 shows seismic networks used to record the P wave RFs in this study without a corresponding DOI are found in Table 1. Seismic networks with a corresponding DOI are detailed in the Open Research section of the main article.

3 Manual Quality Control

Manual quality control involves visual inspection of RFs accepted by automatic quality control to identify low quality RFs clearly contaminated by long-wavelength noise (Figure 1). The source of this noise appears only on the radial component seismogram,

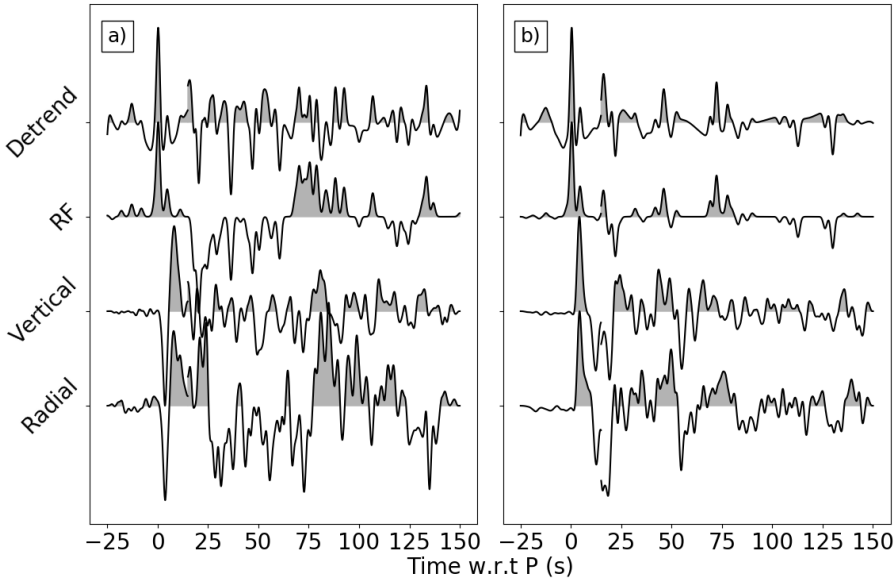

Figure 1. A poor quality (a) and accepted (b) receiver function (RF) identified by visual inspection with the corresponding vertical and radial component seismograms filtered to 0.01-0.4 Hz and the same RF detrended using a 5^{th} order spline. All traces are amplified by a factor of 3 between 15-150 s.

but is not constrained to any particular seismic stations. Whilst a 4^{th} or 5^{th} order sinusoidal spline is capable of removing the long wavelength noise from these RFs, higher frequency noise remains that is indistinguishable from the seismic signals of interest. RFs are only removed where clear high amplitude noise is present, affecting ~10% of RFs that pass automatic quality control.

4 Data Distribution

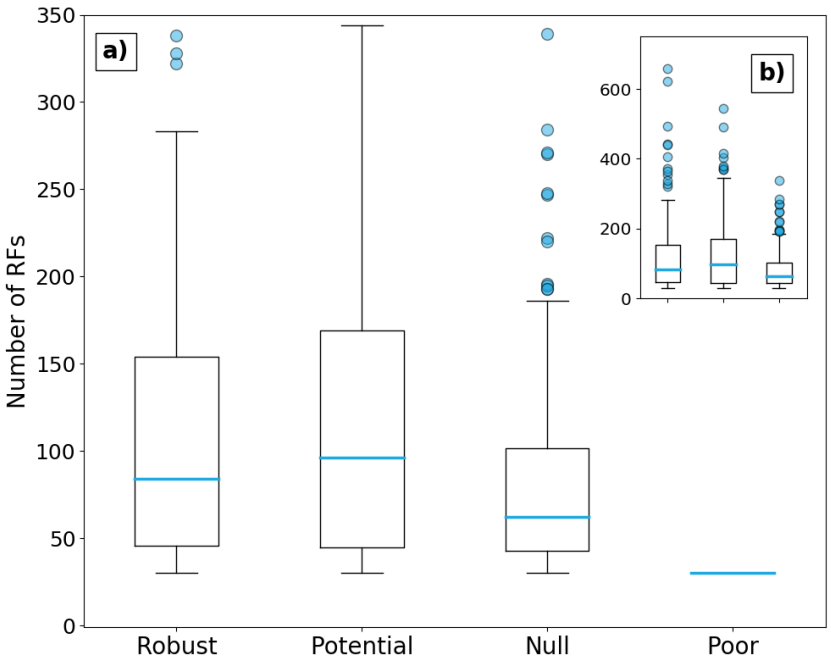

Figure 2. Box plots of the number of RFs for each classification of stack in Figure 5 with a) zoomed to show all non-outlying values and b) showing the full range of the data. The blue line represents the median number of receiver functions for each classification, with the box extending from the 25^{th} to the 75^{th} percentile. Outliers are marked with blue circles.

Using a large data set presents the opportunity to study the impact of data distribution on the resulting stacks and maps. Here we consider the impact of the number of RFs, and the epicentral distance and backazimuthal distance distribution of RFs.

Reassuringly, the number of RFs in a stack has little bearing on the classification of the stacks with robust, potential and null stacks having median values of 84 RFs, 96.5 RFs, and 62.5 RFs respectively. It can also be seen that there is significant overlap in

the interquartile range for each classification of stack (Figure 2). Comparison is not made to the sole poor quality stack.

Backazimuth standard deviation is a measure of the spread of backazimuths for a single stack, calculated using the circular standard deviation. When comparing the presence of phases in the depth range for the X (depth stack only) and the standard deviation of backazimuth (σ) in Figure 3, it is apparent that the two are anti-correlated. Though this anti-correlation is weak (ρ = -0.42), it can be seen in several regions that a reduction in σ is accompanied by an increase in normalised vote for arrivals in the depth range of PXs and is as great as -0.64 for Madagascar and the Indian Ocean region. There are two potential causes of this anti-correlation: topography on the X, and/or the influence of epicentral distance distribution.

If topography exists on the X, then stacks with small standard deviation in backazimuth are less likely to be sensitive to this, especially if stacks are dominated by arrivals at one station. Using stacks with large numbers of RFs ($\geq$100), RFs can be subdivided into four quadrants of backazimuth (Figure 4) to analyse whether topography occurs across the X. Finding the circular mean, four quadrants can be designated such that the dominant backazimuth of data is not divided into multiple bins (Figure 4a). For most RF stacks, this results in one quadrant with most RFs, and three others with few to none, thus being unusable for this analysis. Figure 4 shows an example with sufficient data in more than one bin (Figures 4d-g, j and k). Stacking all RFs for this bin shows an X arrival (Figures 4b and c), though it is somewhat streaky with data looking to have come from epicentral distances >70°. Splitting the stack into four quadrants reveals a high quality X observation in data approximately from the East (Figures 4f and g) at 276 km depth, two potential X observations in data from the north (Figures 4d and e) and west (Figures 4j and k) at 281 and 297 km depth and a poor quality stack with data from the south (Figures 4h and i). It is clear the overall stack (Figures 4b and c) is dominated by data from the west (Figures 4j and k) with >70% of RFs coming from this backazimuthal quadrant which shows the streaky X arrival at 297 km depth. While the data from the west (Figures 4j and k) would be classified as 'Potential' if taken alone, comparison with data from the East (Figures 4f and g) show that >20 km of topography may occur across the stacking regions should this streaky arrival be taken to be the X. This stack also highlights the potential for X observations to be masked by data predominantly sourced from a small epicentral distance range. Epicentral distance distribution is strongly

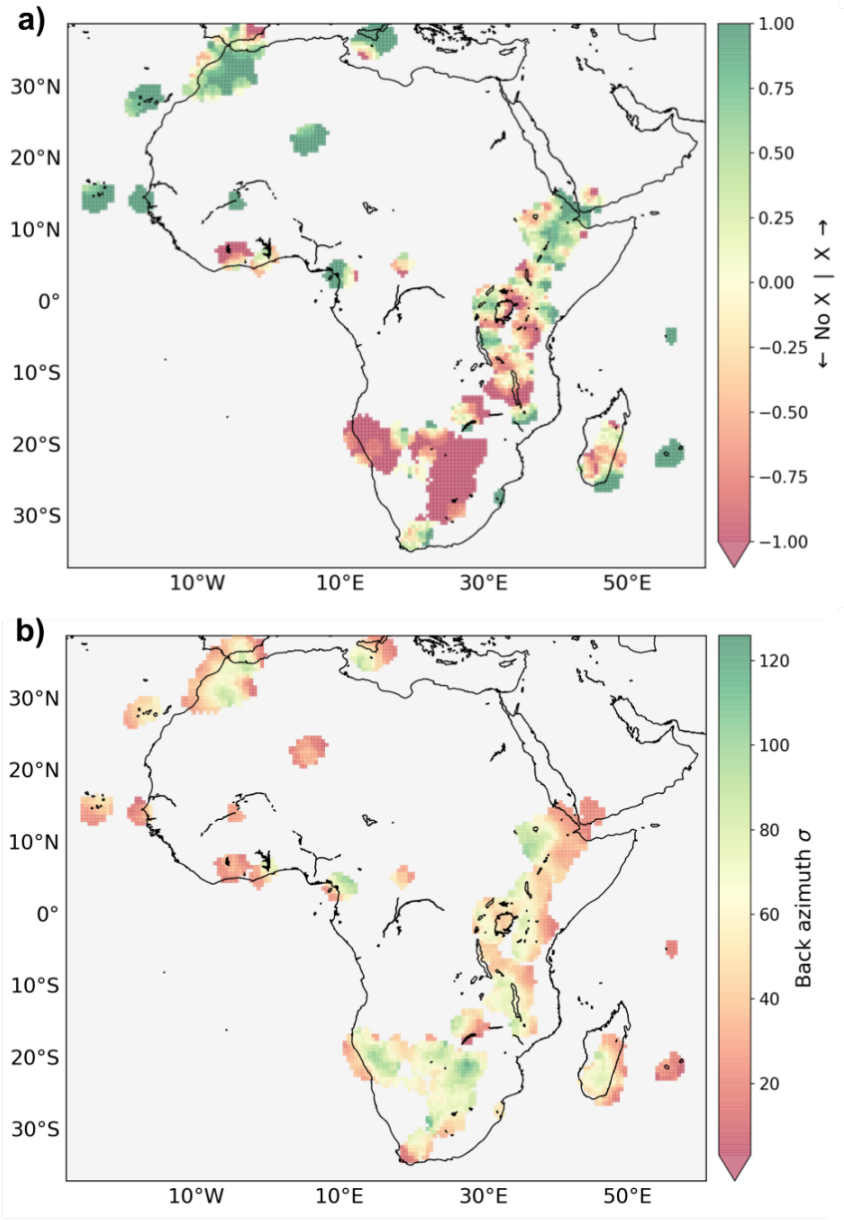

Figure 3. Vote maps of a) X observation in depth stacks and b) standard deviation of backazimuth (σ) for 597 overlapping 1° radius bins with ≥2 votes on a 0.5°x0.5° grid.

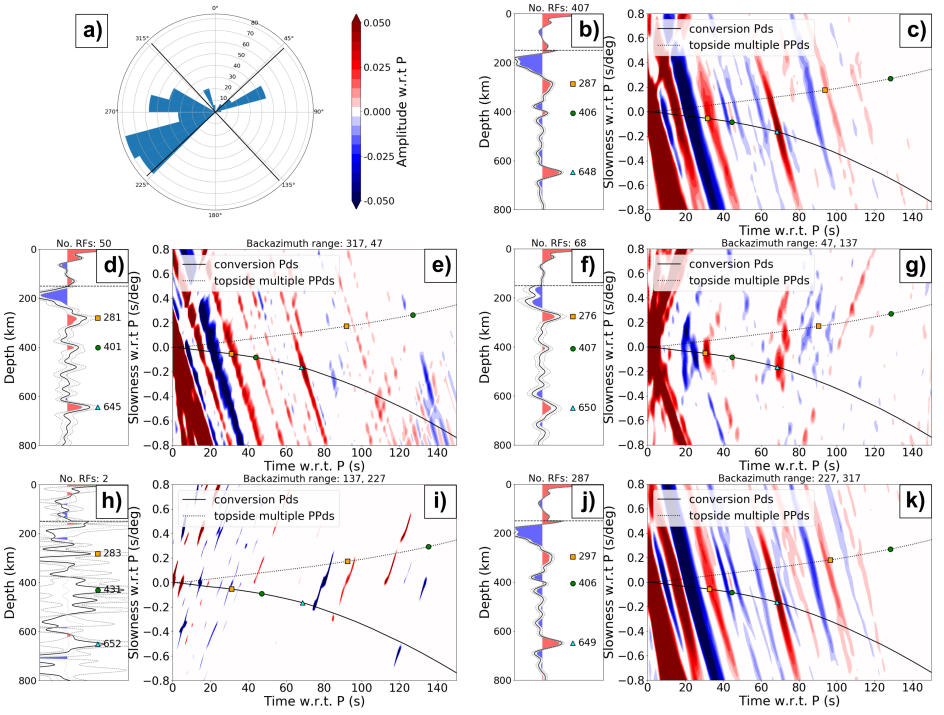

Figure 4. a) Backazimuth distribution of RFs within one bin. Depth (b, d, f, h and j and slowness (c, e, g, i and k) stacks of all data for one bin (b and c) and four quadrants of back-azimuth (d-k) as divided by the thick black lines in a). Stacks are filtered between 0.01-0.4 Hz. Depth stack: Time-to-depth converted RFs are linearly stacked with the black line marking amplitude (normalised to P) and dashed lines marking 2 σ_M. Amplitudes are multiplied by 5 below the horizontal dashed line at 150 km depth. The stack is converted from time-to-depth using SEMUCB_WM1. Coloured symbols mark significant peaks from PXs (orange squares), P410s (green circles), and P660s (cyan triangles). Slowness stack: RFs with amplitude >2 σ_M normalised to P stacked in the time-slowness domain. Predicted time-slowness curves are shown for the direct (Pds) and multiple (PPvds) phases. The coloured symbols correspond to predicted times and slownesses for direct arrivals and PPvds multiples for significant arrivals in the depth stacks computed from PREM.

linked with backazimuth distribution. As for a single backazimuth, it is likely there are only a narrow range of epicentral distances where earthquakes occur due to the sparsity of plate boundaries across Earth's surface.

5 Time-to-depth Conversion

To assess the quality of time-to-depth conversions, receiver function studies often assess the (de-)correlation between 410 and 660 km discontinuity depths (e.g. Dueker & Sheehan, 1998; van Stiphout et al., 2019; Boyce & Cottaar, 2021). Given the polarity of the Clapeyron slopes for the 410 and 660, and assuming the mantle transition zone is dominated by temperature variations, the topography on the 410 and 660 is largely expected to be anti-correlated in the olivine system. Unaccounted for structures in the upper mantle would consistently shift both the 410 and 660 up or down with equal magnitude for fast and slow wavespeed anomalies respectively. A reduction in correlation between 410 km and 660 km topography is used as evidence that a velocity model better accounts for upper mantle velocity structure. The maximum topography and the distribution of topography are also considered to assess how well PREM, SEMUCB_WM1 and AF2019 correct for velocity structure in the African upper mantle.

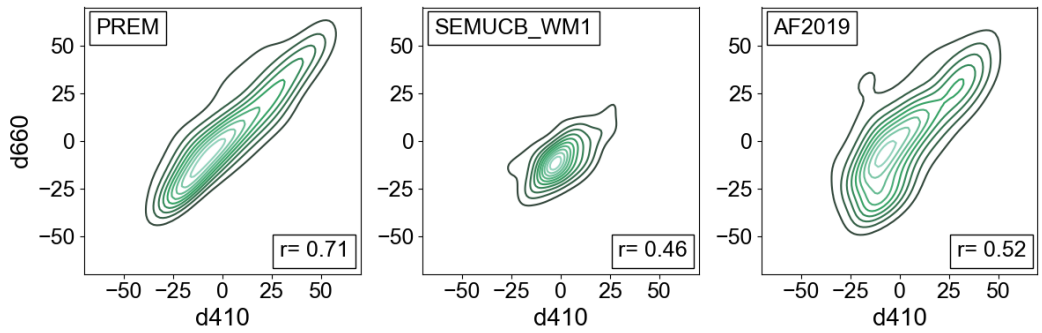

Figure 5. Probability density plots of 410 and 660 km topography for 597 RF stacks depth converted using PREM, SEMUCB_WM1 and AF2019. d410 and d660 are the topography in each stack taken with respect to 410 and 660 km. Pearson's r correlation values are displayed in the bottom right for each model.

1D velocity models are not expected to account for upper mantle heterogeneities and this can be seen in Figure 5 where the d410 and d660 values are strongly correlated

with a Pearson's correlation coefficient of 0.71 and >100 km topography on both the 410 and 660. SEMUCB_WM1 shows the lowest correlation (r=0.46) of the three velocity models suggesting it best accounts for upper mantle velocity structure and can be seen to have the least linear probability density ellipses (Figure 5). Though the correlation of AF2019 (r=0.52) is similar to that from SEMUCB_WM1, topography on both discontinuities is much larger.

The Clapeyron slope of the MTZ discontinuities can be used to estimate total temperature variations across a region. 410 km topography is preferred for this probe as 660 km depths are sensitive to temperature and composition (e.g. Jenkins et al., 2016). Considering an average Clapeyron slope of the 410 km discontinuity of 2.5 MPa/K (Katsura & Ito, 1989; Bina & Helffrich, 1994), the 108 km topography found between stacks using AF2019 would lead to a maximum temperature variation of 1600 K across the region, far greater than the combined temperature anomalies of cold slabs (200-300 K; Cottaar & Deuss, 2016) and hot plumes (150-200 K; Matthews et al., 2016) in the mantle. For the total topography of 76 km between stacks using SEMUCB_WM1, the maximum temperature variation is found to be 1100 K. Although this temperature variation is still larger than expected, SEMUCB_WM1 is preferred for depth correction as temperature variation and topography suggest it better accounts for upper mantle velocity structure. Subsequently, depths reported below are as converted using SEMUCB_WM1.

6 Average upper mantle temperatures of RF stacks

We calculate average upper mantle temperatures between 200-400 km depth for every stack $\pm 1^{\circ}$ latitude and longitude using the temperature deviations found in a geophysical-petrological inversion (Fullea et al., 2021). Histograms in Figure 6 show that Robust observations, distributed across the entire temperature range, are no more likely at elevated mantle temperature than depressed mantle temperatures. However, Null observations are more readily observed at depressed mantle temperatures, potentially linked with widespread Null observations beneath the Kalahari Craton.

7 X-discontinuity relationship to lithospheric thickness

Hoggard et al. (2020) derive lithospheric thickness maps for several tomographic models. Figure 7 shows the distribution of lithospheric thicknesses for three tomographic models SLNAAFSA (A. J. Schaeffer & Lebedev, 2013; A. Schaeffer & Lebedev, 2014;

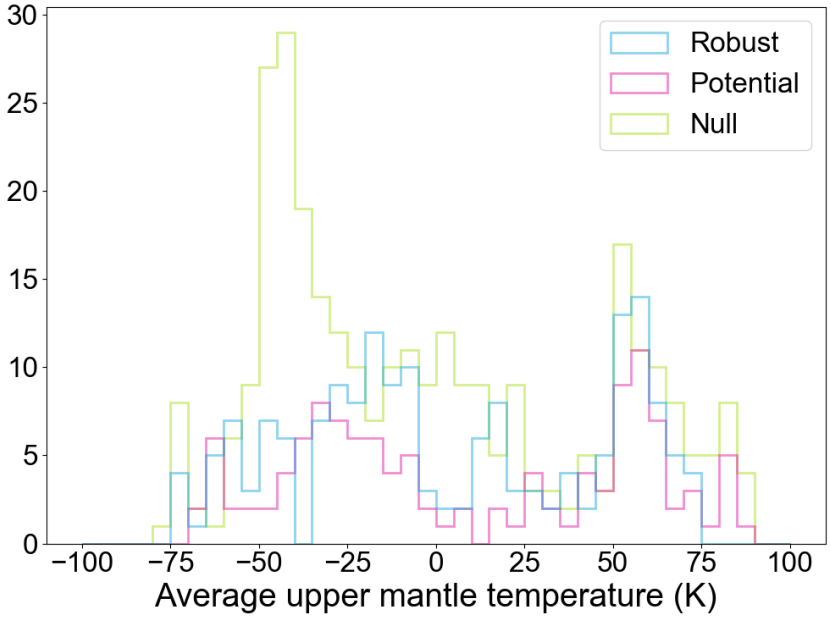

Figure 6. Histograms of the average upper mantle temperature deviations between 200-400 km depth (Fullea et al., 2021) for Robust, Potential and Null stacks.

Celli, Lebedev, Schaeffer, & Gaina, 2020; Celli, Lebedev, Schaeffer, Ravenna, & Gaina, 2020), CAM2016 (Ho et al., 2016; Priestley et al., 2018) and 3D2015-sv (Debayle et al., 2016), for votes corresponding approximately to Robust, Potential and Null categorisations. Votes ≥ 0.5 are mostly clustered beneath lithospheric thicknesses of ≤ 100 km and almost entirely below 200 km, whereas votes $\leq$ -0.5 have maximum concentrations at thicknesses ≥ 120 km with some thicknesses ≥ 200 km for SLNAAFSA.

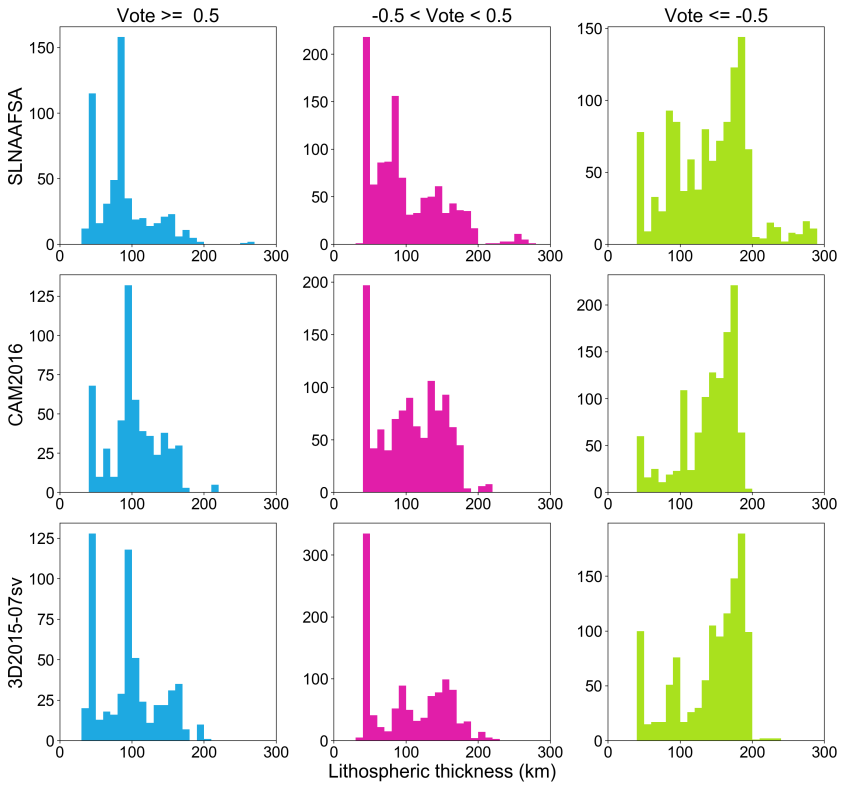

Figure 7. Histograms of the lithospheric thickness in each bin of the vote map (Figure 5) separated into votes for likely X-discontinuity (Vote $\geq$ 0.5), unclear (-0.5 $<$ Vote $<$ 0.5), and likely no X-discontinuity (Vote $\leq$ -0.5) for lithospheric thickness maps derived by Hoggard et al. (2020) from three tomographic models SLNAAFSA (A. J. Schaeffer & Lebedev, 2013; A. Schaeffer & Lebedev, 2014; Celli, Lebedev, Schaeffer, & Gaina, 2020; Celli, Lebedev, Schaeffer, Ravenna, & Gaina, 2020), CAM2016 (Ho et al., 2016; Priestley et al., 2018) and 3D2015-sv (Debayle et al., 2016).

References

Bina, C. R., & Helffrich, G. (1994). Phase transition Clapeyron slopes and transition zone seismic discontinuity topography. *J. Geophys. Res. Solid Earth*, *99*(B8), 15853. Retrieved from `https://doi.org/10.1029/94jb00462` doi: 10.1029/94jb00462

Boyce, A., & Cottaar, S. (2021, March). Insights into deep mantle thermochemical contributions to African magmatism from converted seismic phases. *Geochem. Geophys. Geosyst.*, *22*(3). Retrieved from `https://doi.org/10.1029/2020gc009478` doi: 10.1029/2020gc009478

Celli, N. L., Lebedev, S., Schaeffer, A. J., & Gaina, C. (2020, January). African cratonic lithosphere carved by mantle plumes. *Nat. Commun.*, *11*(1). Retrieved from `https://doi.org/10.1038/s41467-019-13871-2` doi: 10.1038/s41467-019-13871-2

Celli, N. L., Lebedev, S., Schaeffer, A. J., Ravenna, M., & Gaina, C. (2020, January). The upper mantle beneath the South Atlantic Ocean, South America and Africa from waveform tomography with massive data sets. *Geophys. J. Int.*, *221*(1), 178–204. Retrieved from `https://doi.org/10.1093/gji/ggz574` doi: 10.1093/gji/ggz574

Cottaar, S., & Deuss, A. (2016, January). Large-scale mantle discontinuity topography beneath Europe: Signature of akimotoite in subducting slabs. *J. Geophys. Res. Solid Earth*, *121*(1), 279–292. Retrieved from `https://doi.org/10.1002/2015jb012452` doi: 10.1002/2015jb012452

Debayle, E., Dubuffet, F., & Durand, S. (2016). An automatically updated s-wave model of the upper mantle and the depth extent of azimuthal anisotropy. *Geophys. Res. Lett.*, *43*(2), 674–682.

Dueker, K. G., & Sheehan, A. F. (1998, April). Mantle discontinuity structure beneath the colorado rocky mountains and high plains. *J. Geophys. Res. Solid Earth*, *103*(B4), 7153–7169. Retrieved from `https://doi.org/10.1029/97jb03509` doi: 10.1029/97jb03509

Fullea, J., Lebedev, S., Martinec, Z., & Celli, N. L. (2021, March). WINTERC-g: mapping the upper mantle thermochemical heterogeneity from coupled geophysical-petrological inversion of seismic waveforms, heat flow, surface elevation and gravity satellite data. *Geophys. J. Int.*, *226*(1), 146–191. Retrieved

from https://doi.org/10.1093/gji/ggab094 doi: 10.1093/gji/ggab094

Ho, T., Priestley, K., & Debayle, E. (2016, August). A global horizontal shear velocity model of the upper mantle from multimode love wave measurements. *Geophys. J. Int.*, *207*(1), 542–561. Retrieved from https://doi.org/10.1093/gji/ggw292 doi: 10.1093/gji/ggw292

Hoggard, M. J., Czarnota, K., Richards, F. D., Huston, D. L., Jaques, A. L., & Ghelichkhan, S. (2020, June). Global distribution of sediment-hosted metals controlled by craton edge stability. *Nat. Geosci.*, *13*(7), 504–510. Retrieved from https://doi.org/10.1038/s41561-020-0593-2 doi: 10.1038/s41561-020-0593-2

Jenkins, J., Cottaar, S., White, R., & Deuss, A. (2016). Depressed mantle discontinuities beneath Iceland: Evidence of a garnet controlled 660 km discontinuity? *Earth Planet. Sci. Lett.*, *433*, 159–168. Retrieved from https://doi.org/10.1016/j.epsl.2015.10.053 doi: 10.1016/j.epsl.2015.10.053

Katsura, T., & Ito, E. (1989, November). The system Mg_2SiO_4-Fe_2SiO_4 at high pressures and temperatures: Precise determination of stabilities of olivine, modified spinel, and spinel. *J. Geophys. Res. Solid Earth*, *94*(B11), 15663–15670. Retrieved from https://doi.org/10.1029/jb094ib11p15663 doi: 10.1029/jb094ib11p15663

Matthews, S., Shorttle, O., & Maclennan, J. (2016, November). The temperature of the icelandic mantle from olivine-spinel aluminum exchange thermometry. *Geochem. Geophys. Geosyst.*, *17*(11), 4725–4752. Retrieved from https://doi.org/10.1002/2016gc006497 doi: 10.1002/2016gc006497

Priestley, K., McKenzie, D., & Ho, T. (2018). A lithosphere–asthenosphere boundary—A global model derived from multimode surface-wave tomography and petrology. *Lithospheric discontinuities*, 111–123. Retrieved from https://doi.org/10.1002/9781119249740.ch6 doi: 10.1002/9781119249740.ch6

Schaeffer, A., & Lebedev, S. (2014, September). Imaging the North American continent using waveform inversion of global and USArray data. *Earth Planet. Sci. Lett.*, *402*, 26–41. Retrieved from https://doi.org/10.1016/j.epsl.2014.05.014 doi: 10.1016/j.epsl.2014.05.014

Schaeffer, A. J., & Lebedev, S. (2013, April). Global shear speed structure of the upper mantle and transition zone. *Geophys. J. Int.*, *194*(1), 417–449. Retrieved

from https://doi.org/10.1093/gji/ggt095 doi: 10.1093/gji/ggt095

van Stiphout, A. M., Cottaar, S., & Deuss, A. (2019, August). Receiver function mapping of mantle transition zone discontinuities beneath Alaska using scaled 3-D velocity corrections. *Geophys. J. Int.*, *219*(2), 1432–1446. Retrieved from https://doi.org/10.1093/gji/ggz360 doi: 10.1093/gji/ggz360